Magnetic Resonance Imaging 61 (2019) 273–284

Contents lists available at ScienceDirect

Magnetic Resonance Imaging

journal homepage: www.elsevier.com/locate/mri

Original contribution

Diffusion MRI using two-dimensional single-shot radial imaging (2D ss-rDWI) with variable flip angle and random view ordering

Kyle E. Jeong[a,b], Edward W. Hsu[b], Eun-Kee Jeong[a,c,*]

[a] Utah Center for Advanced Imaging Research, University of Utah, Salt Lake City, UT, United States of America
[b] Department of Biomedical Engineering, University of Utah, Salt Lake City, UT, United States of America
[c] Department of Radiology and Imaging Sciences, University of Utah, Salt Lake City, UT, United States of America

ABSTRACT

Purpose: The main objective of this study is to develop a 2D single-shot radial-DWI (2D ss-rDWI) technique to reduce motion artifacts and geometric distortion in DW images.
Method: A diffusion-preparation module is developed and applied prior to the data acquisition. Because the diffusion-prepared longitudinal magnetization is measured over multiple RF excitations in each shot, 2D ss-rDWI is subject to low signal-to-noise ratio (SNR). We used variable-flip angle (VFA), random view ordering (RVO), and sliding spokes, and compared the performances to constant flip angle (CFA), smooth view ordering (SVO), and identical spoke averaging, respectively. For each technique, we performed numerical simulation and MRI experiments on a fluid phantom as well as in-vivo human brain studies with a 3 T MRI system.
Results: Using VFA, optimal SNR was acquired for 2D ss-rDWI. Using SVO, the high signal is clustered at specific quadrant in 2D k-space: the first quadrant using high initial flip angle or the last quadrant using the low flip angle. This clustered signal in k-space led to geometric distortion in image space. 2D ss-rDWI using RVO spreads the high signaled spokes over all angular directions and removes the view-order-related distortion. The in-vivo images using 2D ss-rDWI with VFA and RVO show no geometric distortion at the skull base brain, but greatly reduced SNR compared with those using 2D ss-DWEPI.
Conclusion: 2D ss-rDWI is optimized by using VFA with RVO. The resultant DWI using 2D ss-rDWI is insensitive to motion-induced artifacts and geometric distortion. Even with low SNR, it may be useful for DWI of organs limited by severe susceptibility-induced geometric distortion.

1. Introduction

Diffusion-weighted MRI (DWI) is a powerful imaging method used to probe the random motion of water molecules in biological organs. Additionally, diffusion-tensor MRI (DTI) provides information about the direction of the background structure and diffusivities in the local symmetry system. For reliable diffusion MRI, particularly for quantitative imaging of DWI, one must produce DWI free of motion artifacts and geometric distortion. Conventional multi-shot-based DWI is not commonly used because of motion-induced artifacts caused by inconsistent phase-error in the measured signal due to the coupling between the applied diffusion gradient and subject's physiological motion [1–3]. Therefore, 2D single-shot diffusion-weighted echo-planar imaging (2D ss-DWEPI) is commonly used for data acquisition [4–6].

While able to ameliorate motion artifacts, 2D ss-DWEPI is vulnerable to geometric distortion induced by the field inhomogeneity [4], particularly at tissue/air and tissue/bone interfaces, due to differences in magnetic susceptibility. A pixel signal with off-resonance frequency shifts toward the direction with lower effective bandwidth, typically along the frequency-encoding direction, except in EPI-type acquisition where the distortion is along the phase-encoding direction. Therefore, DWI using the conventional single-shot EPI-based acquisition is limited to intra-cranial brain, far from the sinus and temporal bone [1,7,8]. Although multi-shot DWI acquisition, such as 'MUSE' approach [6],

Abbreviations: 2D ss-rDWI, 2D single-shot radial-DWI; NMR, nuclear magnetic resonance; FID, free induction decay; RF, radio frequency; FOV, field of view; DWI, diffusion-weighted imaging; DTI, diffusion tensor imaging; rDWI, diffusion-weighted MRI using radial sampling; RVO, random view ordering; SVO, smooth view ordering; CFA, constant flip angle; VFA, variable flip angle; SNR, signal-to-noise ratio; MTF, modulation transfer function; PSF, point spreading function; ACQ, acquisition; TM, mixing time; TR, repetition time; TE, echo time

* Corresponding author at: Department of Radiology and Imaging Sciences, Utah Center for Advanced Imaging Research (UCAIR), University of Utah, Salt Lake City, UT 84108, United States of America.
E-mail address: ek.jeong@utah.edu (E.-K. Jeong).

https://doi.org/10.1016/j.mri.2019.04.008
Received 6 February 2019; Received in revised form 21 March 2019; Accepted 17 April 2019
0730-725X/ Published by Elsevier Inc.

PROPELLER [9], and readout-segmented EPI [10], produces DWI with greatly reduced geometric distortion, complete removal of the phase-error with high consistency is required.

Although there have been other single-shot DWI and DTI techniques using non-Cartesian sampling, such as spiral imaging [11,12], we developed a general-use 2D single-shot DWI with radial sampling (2D ss-rDWI) technique [13]. Due to heavy sampling at the k-space center and the effect of motion artifact distributed in two different dimensions rather than one, radial MRI is insensitive to motion-induced ghosting artifact [2,14]. Complete coverage of k-space after a single diffusion-preparation, i.e., single-shot acquisition, further freezes any physiologic motion during the acquisition [15]. Furthermore, unlike 2D ss-DWEPI acquisition, 2D ss-rDWI is substantially less sensitive to susceptibility-induced geometric distortion. However, the major disadvantage of 2D ss-rDWI is its relatively low SNR, a result of the diffusion-prepared longitudinal magnetization being measured over multiple excitations – T_1-decay and consecutive usages along the echo train result in a weak signal.

This paper presents several techniques that improve 2D ss-rDWI by increasing the SNR using variable flip angle scheme and reducing the geometric distortion by uniformly distributing the transverse magnetizations on the 2D k-space. First, variable flip angle (VFA) over the echo train is employed to equalize the transverse magnetization of each subsequent spoke as the flip angle is gradually increased [16]. Second, random view ordering (RVO) is used to randomize the blurring effect inherent in conventional ss-DWI. Furthermore, as diffusion MRI typically requires multiple averages to increase the SNR, each average shot of 2D ss-rDWI covers different radial spokes and its magnitude is averaged in image domain to generate images with reduced streak artifact, which is intrinsic in the conventional undersampled radial MRI [17,18].

2. Materials and methods

2.1. Pulse sequence

Manufacturer's 2D radial sequence was modified to adapt (i) diffusion-preparation before a train of radial data acquisition, (ii) VFA scheme, and (iii) RVO, using pulse sequence development software (IDEA). All experiments were performed with a whole body 3 T MRI system (Prisma, Siemens Medical Solution, Erlangen, Germany), of which maximum strength of the diffusion gradient is 80 mT/m and gradient slew-rate 200 mT/m/s.

The diffusion-preparation module was developed and applied prior to each single-shot acquisition, as illustrated in Fig. 1a. The dephasing crusher gradient $G_{cr}{}^{d}$ induces the diffusion-prepared magnetization within a imaging voxel more than 2π, which then is restored back to the longitudinal space by the tipup 90° RF pulse [16]. The dephasing crusher gradient $G_{cr}{}^{d}$, which include the first half of the slice-selective gradient for the tip-up 90° RF pulse. A rephasing crusher gradient $G_{cr}{}^{r}$ is used to selectively measure the diffusion-prepared magnetization only, while spoiling the freshly recovered magnetization during the delay between the diffusion preparation and the excitation RF pulses. To minimize the echo time, the rephrasing crusher $G_{cr}{}^{r}$ and refocusing gradient G_{ref} added together after each excitation RF (indicated by blue shaded trapezoid).

The data acquisition, which is enclosed by curly red parenthesis {}, is based on a spoiled gradient-echo (GRE) imaging with radial sampling without steady-state, i.e., spoiling both the transverse and recovering longitudinal magnetizations. Timings were carefully adjusted to position the peak of imaging echoes at the stimulated-echo position after each excitation RF pulse α_n.

Fig. 1b indicates gradually increasing flip angles in VFA scheme. Flip angle α_n of the $n^{\underline{th}}$ RF pulse is calculated using Eq. [2] for a given T_1 value. Although this algorithm depends on specific T_1 relaxation time, as indicated by eq. [2], the effect is broad using RVO for T_1 ranging 0.4–1.5 s, which is demonstrated in Fig. 3b.

2.2. Viewordering

Entire spoke directions are prepared and segmented to desired number of shots to make each shot uniformly covering the 2D k-space with sliding radial views from other shots. For instance, as illustrated in Fig. 2a, 360° plane is divided to 24 radial lines with θ = {0°, 15°, 30°, 45°, …, 345°} and then regrouped to three SVO shots (A, B, C) of eight radial spokes, A = {0°, 45°, 90°, …, 315°}, B = {15°, 60°, 105°, …, 330°}, C = {30°, 75°, 120°, …, 345°}. For RVO, each SVO is randomly shuffled within each single-shot, for instance, {180°, 0°, 225°, 315°, 135°, 45°, 270°, 90°}, {150°, 285°, 60°, 240°, 15°, 195°, 105°, 330°], {210°, 75°, 255°, 30°, 345°, 165°, 300°, 120°}. The numbers in Fig. 2(b–d) indicate the orders along an echotrain.

2.3. Variable flip-angle scheme

The longitudinal magnetization after a diffusion-preparation ($[90^{\circ} - G_D - 180^{\circ} - G_D - 90^{\circ}] - G_{spoil}\cdots TM_o\cdots - \alpha_1$) is the sum of decaying diffusion-weighted and freshly recovering magnetizations, of which a brief derivation is described in Appendix 1,

$$M_z(t) = M_z^D(0)e^{-\frac{t}{T_1}} + M_o\left(1 - e^{-\frac{t}{T_1}}\right). \quad (1)$$

Here, M_o, $M_z^D(t)$, and t indicate the fully-recovered thermal and diffusion-weighted magnetizations, and the time between diffusion-preparation and an investigatory RF pulse, respectively. The imaging

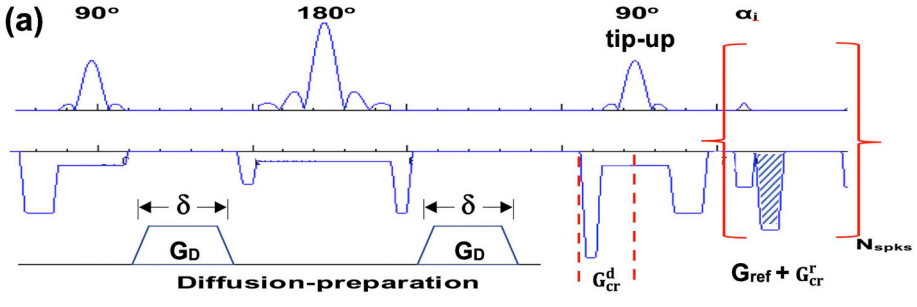

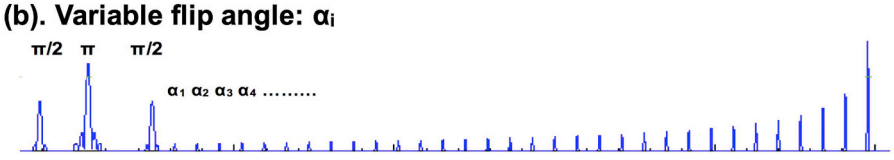

Fig. 1. (a). Diffusion-preparation, and (b) variable flip angle scheme. The diffusion-prepared magnetization is selectively measured by using a pair of dephasing and rephasing crusher gradient pulse $G_{cr}{}^{d}$ just before the tip-up 90° and $G_{cr}{}^{r}$ immediately after each excitation RF pulse α_i, while spoiling the freshly recovered magnetization during the mixing time. Zero$^{\underline{th}}$ moment of $G_{cr}{}^{d}$ is the same as that of $G_{cr}{}^{r}$. Note that the shaded gradient after the excitation RF pulse α_i, labeled as $G_{ref} + G_{cr}{}^{r}$, includes the rephasing crusher $G_{cr}{}^{r}$ and refocusing gradient of the slice-selection gradient.

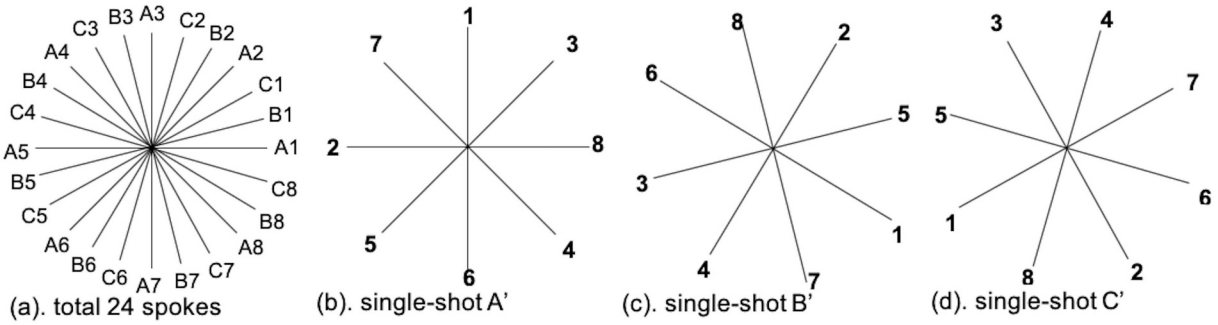

Fig. 2. Viewordering scheme: 24 total spokes in (a) are divided to three SVO shots A, B, and C, of which each group uniformly covers the 2D k-space but is rotated with respect to other shots. Each set of SVO spokes is randomly shuffled for RVO scheme (single-shots A', B′, C′), as the numbers in (b, c, d) indicate the order along an echotrain.

acquisition needs to measure only the diffusion-prepared magnetization (the first term), while spoiling the freshly recovering magnetization (the second term). During the delay time t, $M_z^D(t)$ undergoes a T_1 decay, as in the first term of Eq. [1], until its partial fraction is investigated by an imaging excitation RF pulse. Further, it is gradually decreased by consecutive applications of excitation RF pulses, i.e., α_n pulses, over the echo train. Therefore, using the conventional constant flip angle excitation, the available transverse magnetization M_+^D decreases for later FID data.

In principle, a geometric distortion is anticipated by how the NMR echoes with decaying signal intensities are distributed along the angular direction in k-space. In this numerical simulation, we investigate the effect of two acquisition strategies: (i) VFA scheme, of which the flip angle gradually increases to equalize the transverse magnetization for each measurement, and (ii) random view ordering (RVO) to pseudo-uniformly distribute the measured echo data along the angular direction in k-space.

First, the flip angle of the last RF pulse is set to 90° to consume all diffusion-prepared magnetization before the next acquisition. Then, the flip angle of previous RF pulse is calculated using [18],

$$\tan\alpha_{n-1} = \sin\alpha_n e^{-\tau/T_1} \tag{2}$$

The $n^{\underline{th}}$ projection data is weighted by $e^{-(TM_o+n\tau)/T_1}\cos^n\alpha_n$ according to the measurement time ($TM_o + n\tau$) after diffusion-preparation. Here, TM_o, τ, and α_n indicate minimum mixing time between the peaks of tip-up RF pulse in the preparation and the first excitation RF pulse, echo spacing between two consecutive excitation RF pulses, and flip angle of $n^{\underline{th}}$ RF pulse, respectively. As indicated in Eq. [2], the algorithm depends on T_1 relaxation time. With shorter T_1, which induces more rapid signal decay along the echotrain with increased waiting time until the partial excitation, the optimal initial flip angle α_1^{opt} needs to be smaller than that for the longer T_1 in order to leave enough magnetization for later acquisitions. In the simulation, we set $T_1 = 1.0$ s, $\tau = 0.003$ s, and total number of projections = 192 (4 shots of $N_\theta = 48$ single-shot spokes), of which α_1^{opt} is calculated as 7.5°.

The projection angle increases linearly with spoke number in smooth view ordering (SVO), while that randomly jumps for RVO. In SVO using constant flip angle (CFA), the signal intensity in the measured echoes decreases in angular direction in the k-space.

2.4. Point-spread function (PSF) analysis

PSF analysis can be used to understand how the different flip angle and view ordering schemes induce the artifacts. PSF can be obtained by the Fourier transformation of the modulation transfer function (MTF), which represents the transverse magnetization along an echo train. A datapoint on a FID travels along a circular path in the 2D k-space of the 2D radial data, of which a constant amplitude is desired to generate an ideal PSF with a single narrow peak. 2D PSF in polar coordinate is described as [19,20],

$$PSF(r,\theta) = \int_0^{\infty} k_r dk_r \int_0^{2\pi} MTF(k_r,k_\phi) e^{-i2\pi r k_r \cos(\phi-\theta)} d\phi. \tag{4}$$

which can be numerically evaluated by summing $MTF(k_r,k_\phi)$ along entire k-space trajectories as [21],

$$PSF(r,\theta) = \Delta k\ \Delta\phi \sum_{m'=0}^{nPnts-1} m'\Delta k_r \sum_{m=0}^{ETL-1} MTF(k_r,k_\theta) e^{-i2\pi r k_r \cos(\theta - m\Delta\phi)}. \tag{5}$$

2D PSF simulation was performed using eq. [5] for various initial flip angles $\alpha_1 s$, ranging from 2.5° to 12.5°, and relative shear shift and SNR were estimated. 1D PSF analysis was also performed and results are presented in Appendix A2. Angular profiles of PSF are illustrated in Fig. 3a for VFA with three different $\alpha_1 s$ (5.5°, 7.5° and 9.5°) and CFA with $\alpha = 7.5°$. Green dots and line for VFA with the initial flip angle α_1^{opt} and SVO and RVO, respectively, indicate no distortion. Any flip angle scheme, which may result in the varying amplitude of $M_+(\alpha_n)$ along the echo train, induces positional shift; e.g., increasing $M_+(\alpha_n)$ by $\alpha_1 < \alpha_1^{opt}$, such as $\alpha_1 = 5.5°$ (red ○) or decreasing $M_+(\alpha_n)$ by $\alpha_1 > \alpha_1^{opt}$ or CFA scheme, e.g., VFA with $\alpha_1 = 9.5°$ or CFA with 7.5°. This shift may be caused by abrupt change in the signal intensity at $k_\theta = 0°$ line. Fig. 3b, in which the amount of shift is plotted with respect to the initial flip angle $\alpha_1$in VFA and α in CFA, illustrates minimal distortion using VFA with $\alpha_1 = \alpha_1^{opt}$. The shift monotonically increases with increased flip angle for CFA scheme, as illustrated as (+) in Fig. 3b.

2.5. Numerical simulations

Numerical simulation is performed to evaluate the SNR and image artifact for four combinations of flip angle and view order schemes in 2D ss-rDWI. A simulation software was developed using Python 3.x language, particularly SymPy [22] for symbolic calculation, NumPy [23] and SciPy [24] for array processing, and matplotlib [25] for plotting and displaying data. The software generates a synthetic 2D image that includes multiple internal structures with different T_1 relaxation times (0.4, 1.0, 1.5, and 5.0 s), signal intensities, and off-resonance local fields. This synthetic image is rotated for a specific projection angle and its projection is measured in complex number.

Fig. 4 illustrates the simulated images using different combinations of initial flip angle α_1 and view-orderings. The square structures in the synthetic image are sheared in the angular direction toward the spokes with large signal intensity as shown in Figs. 4(iii-a, iii-c) using the SVO, but not using RVO as shown in Figs. 4(iii-b, iii-d). With VFA using an optimal flip angle α_1^{opt}, SVO also produces distortion-free image, as in Fig. 4(ii-a).

CFA scheme with flip angle smaller than α_1^{opt} produces distortion-free images using either SVO or RVO, however, the signal intensity is

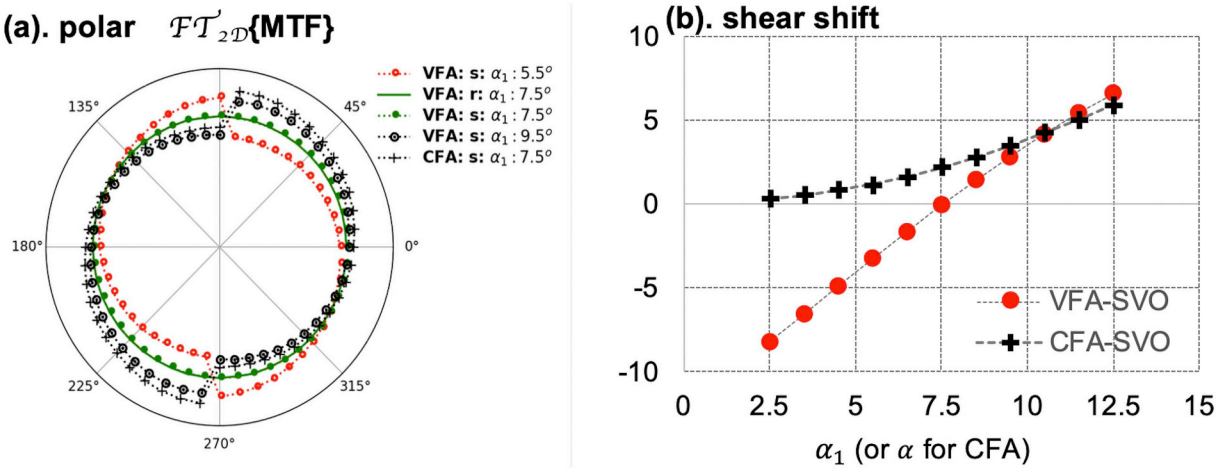

Fig. 3. (a) 2D polar FFT of the MTF for the VFA with different initial flip angle α_1 (red ○, black ◎, green ●) and CFA with $\alpha = 7.5^o$ (+), and (b) plot of the relative shift vs. α_1 of VFA (red ●) and CFA (+) schemes with smooth view ordering. In (a), the deviation from the green trace with $\alpha_1^{opt} = 7.5^o$ indicates the positional shear along the angular direction. Note that the shear direction is reversed about the $\alpha_1 = \alpha_1^{opt}$ for VFA, while it continues increasing for CFA scheme, as shown in (b). (For interpretation of the references to colour in this figure legend, the reader is referred to the web version of this article.)

smaller as the flip angle deviates further from α_1^{opt}, because the diffusion-prepared longitudinal magnetization is not fully consumed in each shot unlike the VFA scheme.

2.6. Averaging identical spokes vs. sliding spokes

Each single-shot consists of a finite number of radial spokes, say 48, and a multiple averaging acquisition is needed to improve the SNR. In conventional Cartesian MR imaging, the identical k-space coverage is performed for averaging. For radial imaging, particularly with undersampled acquisition, it is more desirable to use different k-space coverage at different single-shots. However, radial sampling with identical spoke directions for all average shots covers sparsely at high spatial frequency in k-space. Here, the effect by identical and sliding k-space coverage is numerically simulated for total 384 spokes with 8 single-shots of 48 spokes. For averaging of identical spokes, each shot covers the same spoke directions, while that slides along the angular direction in sliding averaging. Fig. 5b and c are numerically simulated radial images of the original synthetic image in Fig. 5a, using 8 averages of identical and sliding spokes, respectively. Fig. 5c using the sliding spokes clearly mimics the original image in Fig. 5a, while that using identical spokes in Fig. 5b shows noticeable artifact, of which pattern depends on the internal structure of the object.

2.7. MRI experiment

MRI experiments were conducted on a phantom, which consists of four cubic boxes filled with 0.0, 0.067, 0.10, and 0.025 mM $[Mn^{2+}]$/distilled water solutions, and an ex-vivo lamb heart using the manufacturer's receive-only 20 channel head RF coil. Using an inversion-recovery spin-echo MRI, the proton T_1 relaxation times of each concentration were estimated as 4.0, 1.5, 1.0 and 0.4 s, respectively [2,3]. For each comparison experiment, acquisition parameters were kept except for the flip angle and view-order. For RVO and SVO, both CFA

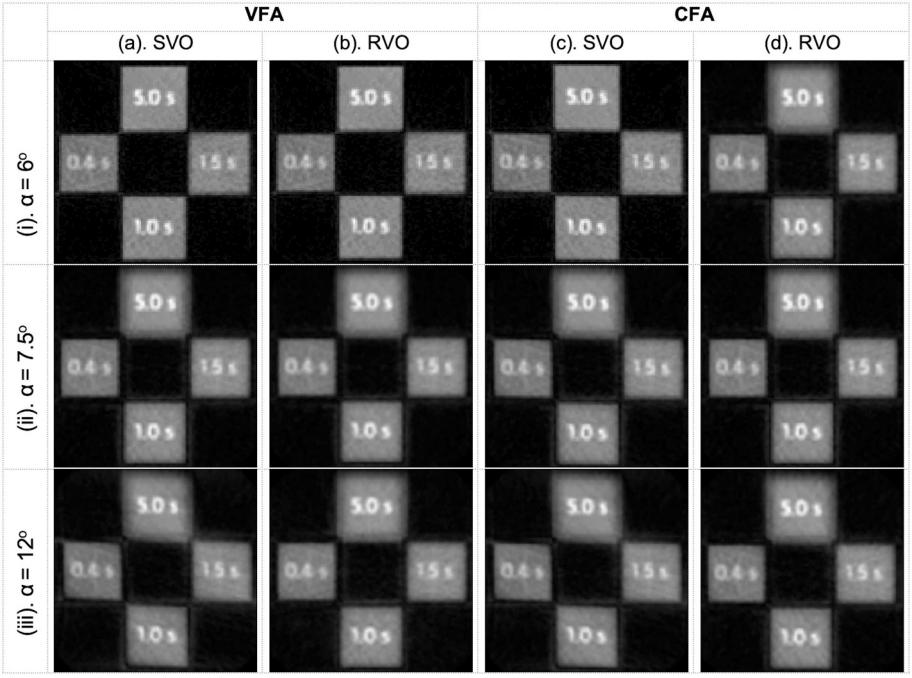

Fig. 4. The numerically constructed images of a synthetic image using different flip angles ((i) 6°, (ii) 7.5°, (iii) 12°) with smooth and random view orderings for (a, b) variable and (c, d) constant flip angles. Each square box has different T_1 relaxation time (0.4, 1.0, 1.5, 5.0 s), as engraved. The geometric distortion is caused by clustering the high signal projection into specific projection angles. The shearing distortion is corrected by randomizing the view order for both VFA and CFA (columns b and d). As the initial flip angle deviates away from the optimal initial flip angle α_1^{opt}, simulated radial images with smooth ordering show increased shearing distortion, which the random view ordering greatly reduces.

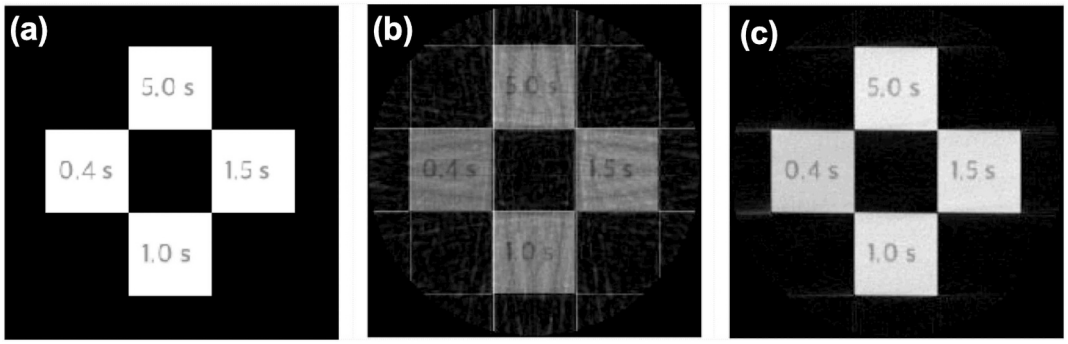

Fig. 5. (a). Original synthetic image, and averaged images using 8 shots of (b). identical 48 radial spokes and (c). sliding 48 radial spokes. Residual horizontal line in (c) may be caused by the specific internal structure of this synthetic image with abrupt change between the object and background signals. This residual artifact was decreased with increased number of spokes (not shown).

and VFA schemes with different initial flip angles were applied. For all phantom experiments, we used receiver bandwidth 1085 Hz/pixel, 3 ms echo spacing, 128 sampling points (N_r) with oversampling factor 2, i.e., 256 actual samples, TR 3.0 s, FOV 256 mm and 4 mm thickness, and magnitude averaging of eight single-shots of 48 spokes. Note that the minimal number of radial spokes is $N_\theta{}^N = \pi N_r/2$ by Nyquist sampling theorem for a half-π projection, e.g., $N_\theta{}^N = 100$ for $N_r = 128$.

To investigate the signal behavior of specific flip angle schemes along an echo-train of stimulated echoes, an MRI experiment was conducted using variable initial flip angles α_1 and constant flip angle of $\alpha = 7.5^\circ$, comparing RVO and SVO schemes. FID signal intensity was measured at k = 0. The initial flip angle α_1 was set to 6.0°, 6.5°, 7.0°, 7.5°, 8.0°, 8.5°, and 9.0° with $\alpha_{last} = 90^o$. Note that the optimal initial flip angle $\alpha_1{}^{opt}$ is calculated as 7.5° for VFA with $\tau/T_1 = 0.003$ and 48 spokes.

Four acquisition protocols were compared: RVO with VFA, SVO with VFA, RVO with CFA, and SVO with CFA. All four protocols shared identical acquisition parameters other than view ordering and flip angle schemes with b-values = 0 and 500 s/mm^2 with δ = 10 ms. Three different α_1s (6°, 7.5°, 9°) were applied for VFA, and $\alpha = 7.5^\circ$ for CFA. For VFA with non-optimal α_1, nth RF flip angle is recalculated using $\alpha_n = \alpha_n{}^{opt} + (\alpha_1 - \alpha_1{}^{opt}) * (90^\circ - \alpha_n{}^{opt})/(90^\circ - \alpha_1{}^{opt})$, which ensures that the last flip angle will be 90°. To compare sliding spokes with identical spoke coverage, an additional imaging experiment was performed to acquire 8 averages of 48, (a) sliding and (b) identical spokes with $\alpha_1 = 7.5^\circ$ VFA and RVO. For sliding averaging, each average shot covers different spoke angles.

For imaging of an ex-vivo lamb heart, the acquisition parameters for DTI were FOV = 192 mm, TR = 3000 ms, bandwidth = 1085 Hz/pixel, ten 2.5-mm thick slices with 0.5 mm gap between neighboring slices, b = 0 and 500 s/mm^2, 12 non-collinear diffusion directions, δ = 10 ms, for both 2D ss-rDWI and 2D ss-DWEPI. For 2D ss-rDWI, we used 8 averages of 48 sliding spokes and $\alpha_1 = 7.5^\circ$. Diffusivity of the bulk water was measured with b = 0, 200, 400, 600, 800, and 1000 s/mm^2 using 2D ss-rDWI and 2D ss-DWEPI. Parallel imaging was used for all 2D ss-DWEPI with reduction factor $R = 2$.

2D ss-rDWI was applied to a brain DWI of a volunteer using 32-channel head RF coil, with signed consent form collected and approved by our organization's Institutional Review Board. Imaging parameters are spatial resolution 1.7 × 1.7 × 4 mm^3, TR/TE = 4000/35.5 ms, receiver-bandwidth 1.085 kHz/pixel, 21 slices, and b = 0 and 500 s/mm^2 along head/ft direction. A total of 1280 radial spokes were segmented to 20 shots of 64 radial spokes with the RVO scheme. To compare the performance of the technique, an experiment was performed using VFA with the initial flip angle $\alpha_1 = 6.6^\circ$, which is the optimal for T_1 1.25 s. The experiment was repeated for VFA/RVO with $\alpha_1 = 10^\circ$, CFA/SVO with $\alpha_1 = 6.6^\circ$ and 10°. 2D ss-DWEPI images were also collected with 4 averages using similar imaging parameters as those for 2D ss-rDWI, including receiver bandwidth, spatial resolution, and TR. The acquisition times of each b-value were 80 s for 2D ss-rDWI and 16 s for 2D ss-DWEPI.

2.8. Image reconstruction

The raw data was transferred to an offline computer and reconstructed using a home-developed reconstruction software programmed using C++ and Python. NumPy [22] and SciPy [24] packages were used for all array processing. The regridding module was programmed using C++, following the detailed instruction in Ch. 13.2 of Bernstein's book [2], and compiled to generate a shared object for unix OS (Linux and MacOS). The Kaiser-Bessel regridding kernel was used with the window width 3.0 and β = 4.205 [26–28]. The data was weighted by $1/k_r$ during the regridding. The python package "ctypes" was used to pass the pointers of the input and output data between the Python and the regridding C++ functions. Images are constructed from each single-shot data and averaged in magnitude, not in complex space. Note that complex averaging is generally preferred to improve the SNR; however, it requires a robust correction of the inconsistent phase errors among shot-to-shot, which are induced by coupling between the applied diffusion gradient and subject motion. Therefore, magnitude averaging is generally used in in-vivo human DWI.

3. Results

Fig. 6 shows the signal intensity with respect to different flip angle schemes of simulated and experimental data. Fig. 5a depicts the plots of signal intensities at $k = 0$ of the measured echoes along an echo train with 48 views for VFA with different initial α_1 (6°–9°) and CFA with $\alpha = 7.5^\circ$. The plots clearly behave as predicted by theory and numerical simulation. The signal intensity is almost uniform using VFA with initial flip angle $\alpha_1 = 7.5^\circ$, which is calculated using the eq. [2] for $T_1 = 1.0$ s. Note that CFA imaging will show the decreasing transverse magnetization along the echo train for any flip angle, of which decay increases with increased flip angle. Plots in Fig. 6(b, c) are SNR, measured on simulated images in Fig. 4 and experimental images in Fig. 7, respectively. These SNR-α_1 curves mimic the simulated SNR in Fig. A2c in Appendix 2. Signal intensity is optimal for all angles of VFA scheme with RVO and SVO, while that using CFA approaches to the maximum of VFA at larger flip angle than $\alpha_1{}^{opt}$ of VFA, e.g., $\alpha = \sim 15^\circ$ in this example.

All rDWI images using SVO in Fig. 7 clearly indicate increased image shearing around the rectangular structures with increased flip angle. 2D rDWI using CFA with RVO produces images with the least distortion, as shown in the columns (d) in Fig. 7. 2D ss-rDWI with VFA and $\alpha_1 = 7.5^\circ$ (and 9°, not shown) present images with good quality. Imaging using CFA with RVO shows minimal artifact, however, with non-optimal signal to noise ratio (SNR) compared to VFA-RVO. Although the simulated radial image maintains the high signal intensity

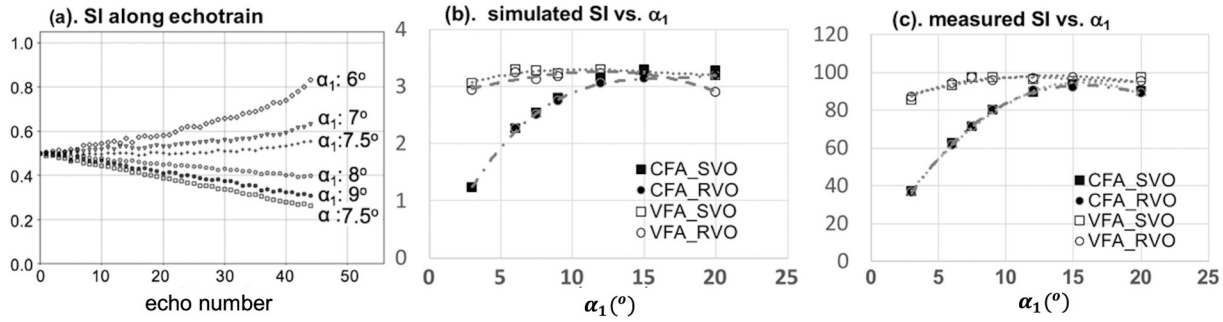

Fig. 6. Signal intensity, measured (a) along an echo train, and at an ROI on (b) simulated images in Fig. 3 and (c) experimental images of a phantom with respect to the flip angle α_1 of the first investigatory RF pulse in flip angle schemes of CFA (■,●) and VFA (□,○). From both simulated and experimental images, VFA provides high signal intensity for broad rage of initial flip angles, while that using CFA approches toward the maximum at larger than $\alpha_1^{opt} = 7.5^o$. The SI curve labeled with $\alpha = 7.5^o$ in (a) indicates for CFA with flip angle 7.5°.

with VFA with large initial flip angle or CFA as shown in Fig. 7(b, c), say $\alpha = \sim 15^o$ in these simulation and experiment, shearing distortion increases with increased deviation of the initial flip angle from α_1^{opt}, as shown in Fig. 4. From this simulation study, we can conclude that 2D ss-rDWI provides optimal images using VFA with RVO scheme and α_1^{opt} calculated for specific T_1. In columns (a, c) of Fig. 7, rDWI using SVO produces images with geometric shearing around each square-shaped structure within the phantom. The square structures are vertically sheared and distorted to appear parallelepiped. These observations are consistent with numerical simulation in Fig. 4, throughout all VFA and CFA schemes. 2D ss-rDWI using CFA and RVO is quite immune to shear distortion. Numerical simulation indicates almost distortion-free rDWI

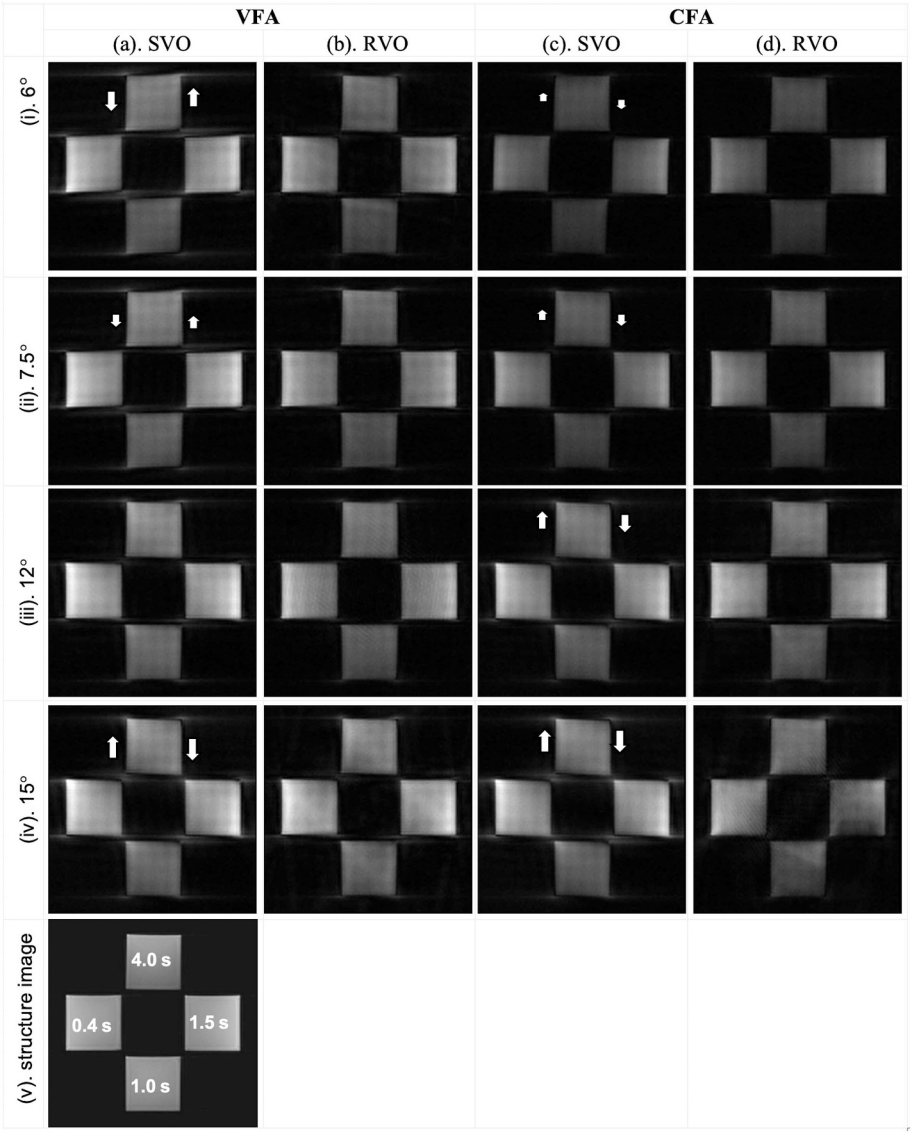

Fig. 7. 2D ss-rDWI of the phantom using (a, c) smooth and (b, d) random view orderings with (a, b) variable and (c, d) constant flip angles. All images, obtained using SVO and VFA with initial flip angle away from 7.5°, are sheared toward clockwise for low FA and counterclockwise for large FA, which are corrected using the RVO. Image in the bottom row is a corresponding structural image, obtained using a gradient-echo MRI. These images are to show the geometric distortion with respect to different combinations of view-ordering and flip-angle schemes. The vertical arrows on selected SVO images qualitatively indicate the degree of vertical shear. All images are displayed using the same window level and width, Therefore, the brightness represents the signal-intensity.

Table 1
Signal-to-noise ratio of two ROIs at b = 500 s/mm^2 measured using ETL = 64. The estimated optimal initial flip angle α_1^{opt} = 6.6° for T_1 1.25 s.

Flip angle scheme	α_1	Vieworder scheme	b = 500 s/mm^2	
			Pituitary gland	Occipital lobe
VFA	6.6°	RVO	30.7	44.1
	6.6°	SVO	33.8	44.3
	10.0°	RVO	29.0	34.7
CFA	6.6°	SVO	20.1	37.9
	10.0°	SVO	24.9	45.5

images using RVO or using low flip angle in CFA scheme. The shear in the images is further decreased using smaller α_1, due to slower decay along the echo train using small flip angle. However, the measured images show about 15% reduction in SNR, compared with VFA-RVO acquisition.

The resultant images from a human brain, that are obtained with several different combinations of flip angle schemes and vieworderings and initial flip angle are shown in Appendix A3. Prabably because of heterogeneity in T_1 relaxation time in human brain, geometric shearing is not obvious, however, SNR is maintained high using VFA compared with CFA, as in the phantom result in Fig. 6. Table 1 lists the SNR measured at pituitary gland and occipital lobe. Although we did not measure as full set of data as the phantom experiment as presented in Fig. 7, it is clear that the SNR is optimal with VFA.

Diffusion-weighted images of an ex-vivo lamb heart are shown in Fig. 8. Fig. 8(c, d) are magnitude-averaged images of eight individual images in Fig. 8(a, b) measured using identical and sliding spokes of 48 spokes, respectively. The inserts indicate total spokes for each averaging acquisition. As predicted by numerical simulation in Fig. 5, the image in Fig. 8c, which was measured using the identical averaging, displays horizontal streaks, which is almost identical to that in the individual images in Fig. 8a. The DWI signals of the bulk-water in a rectangular ROI in Fig. 8e are normalized to that of 2D ss-DWEPI at b = 0 and plotted with respect to b-value in Fig. 8h. Diffusivity measured using rDWI agrees well with that using 2D ss-DWEPI, as $(1.69 \pm 0.12) \times 10^{-3}$ and $(1.71 \pm 0.35) \times 10^{-3}$ mm^2/s for rDWI and DWEPI, respectively. The measured ADC using rDWI shows larger standard deviation than that using DWEPI due to the lower SNR in the source DWIs than DWEPI. Fig. 8g and h are FA-weighted fibermaps using 2D ss-rDWI and 2D ss-DWEPI, respectively. The myocardium is vertically elongated in Fig. 8j because of the geometric distortion due to the magnetic susceptibility, as also shown in the source DW images in Fig. 8g.

Images in Figs. 9 and 10 illustrate DW images and corresponding ADC maps of human brain, measured using (b–d) 2D ss-DWEPI and (e–g) 2D ss-rDWI. The images in Figs. 9a and 10a present anatomic images. DW images, measured using 2D ss-DWEPI in Figs. 9b and 10b, show high SNR but severe geometric distortion at/near air/tissue and bone/tissue interfaces, near the sinus and temporal bone, while images measured using 2D ss-rDWI in Figs. 9e and 10e maintain the shape identical to those of anatomical images in Figs. 9a and 10a. Images in Fig. 10 (b–d), which were measured using 2D ss-DWEPI, illustrate DW images with severe geometric distortion for tissues surrounding the air in the cavernous sinus, including the pituitary gland. This geometric distortion was absent in our 2D ss-rDWI images in Fig. 9(e–g) where the pituitary gland retained its visual structure, although with low SNR. SNRs for 2D ss-DWEPI and 2D ss-rDWI are estimated as 54.3 and 40.5 for Fig. 9 and 52.8 and 41.5 for Fig. 10, at the circular ROI and noise

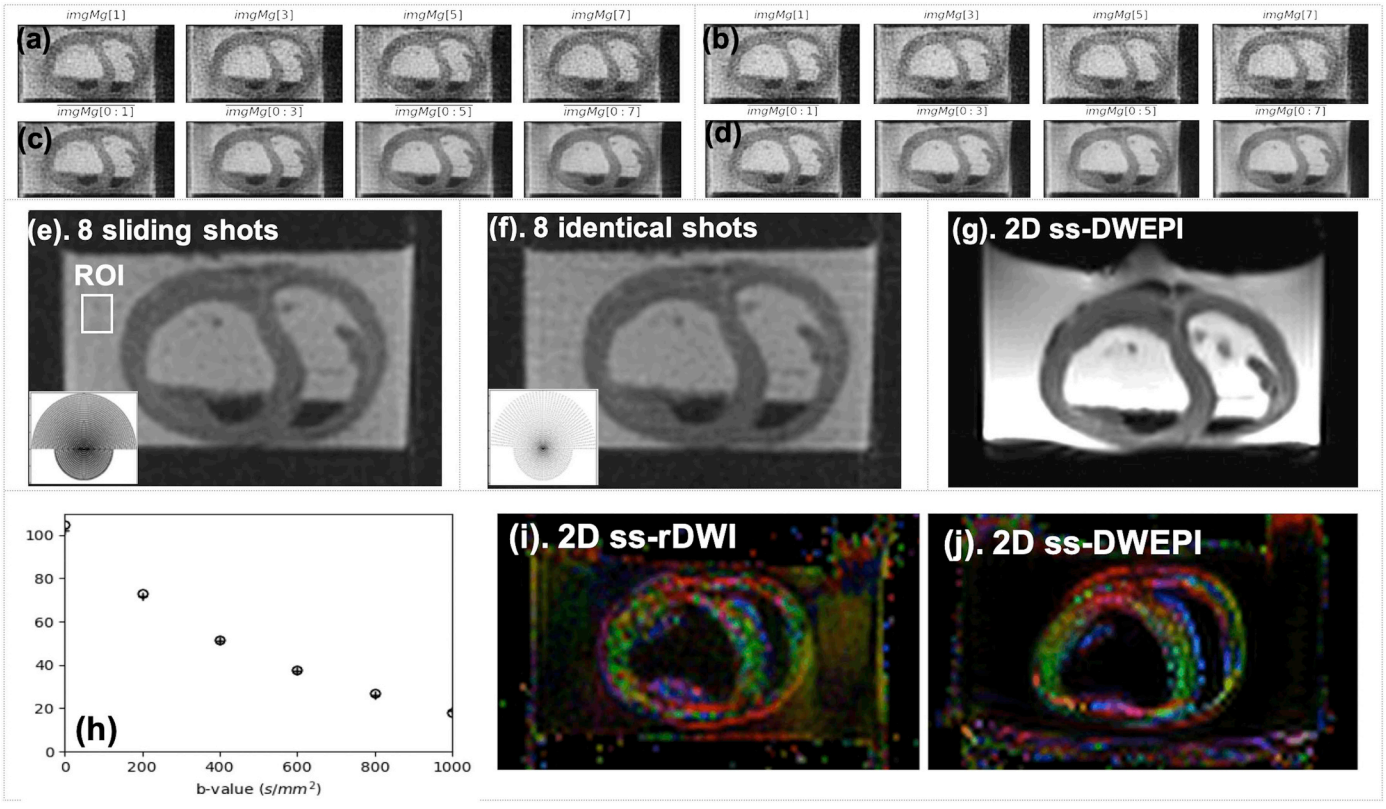

Fig. 8. DWI and DTI of an ex-vivo lamb heart: (a, b) individual and (c, d) progressively magnitude-averaged images of eight single-shot 2D ss-rDWIs (b = 400 s/mm^2) of (a, c) identical and (b, d) sliding coverages, and averaged images of eight (e) sliding and (f) identical radial coverages, (g). conventional 2D ss-DWEPI, (h) signal-b plot of an ROI at PBS for (o) 2D ss-rDWI and (+) 2D ss-DWEPI, and FA-weighted fibermaps of (i) 2D ss-rDWI and (j) 2D ss-DWEPI. Image (f) appears with increased streak artifact in horizontal direction as in the individual images in (a), as expected using low number of data points in the inserted k-space coverages. Note that the images using 2D ss-DWEPI is distorted vertically along the phase-encoding direction. FA-weighted fibermaps in (i, j) look similar to each other.

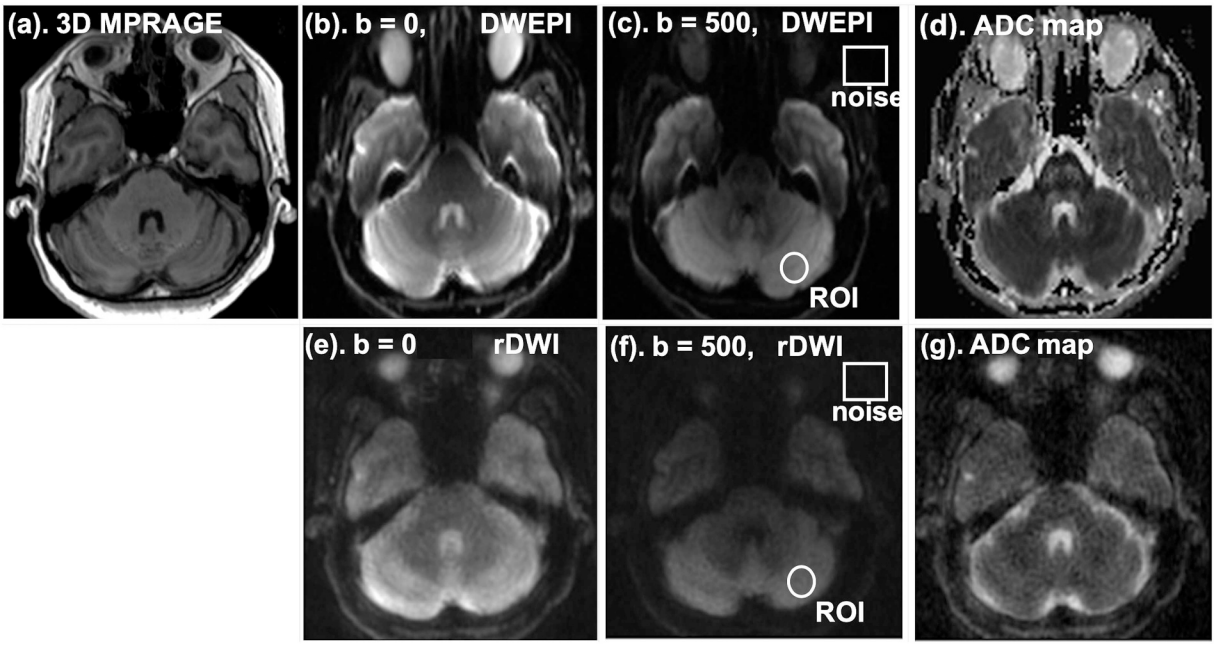

Fig. 9. In-vivo human brain DW images of axial plane: (a) anatomical image, (b–d) 2D ss-DWEPI, and (e–g) 2D ss-rDWI with b = (b, e) 0, (c, f) 500 s/mm^2 and (d, g) corresponding ADC map.. As expected, images measured using 2D ss-DWEPI show severe geometric distortion at the tip of temporal lobes in axial plane and around the sinus. ROIs to estimate the SNR are shown in (c) and (f).

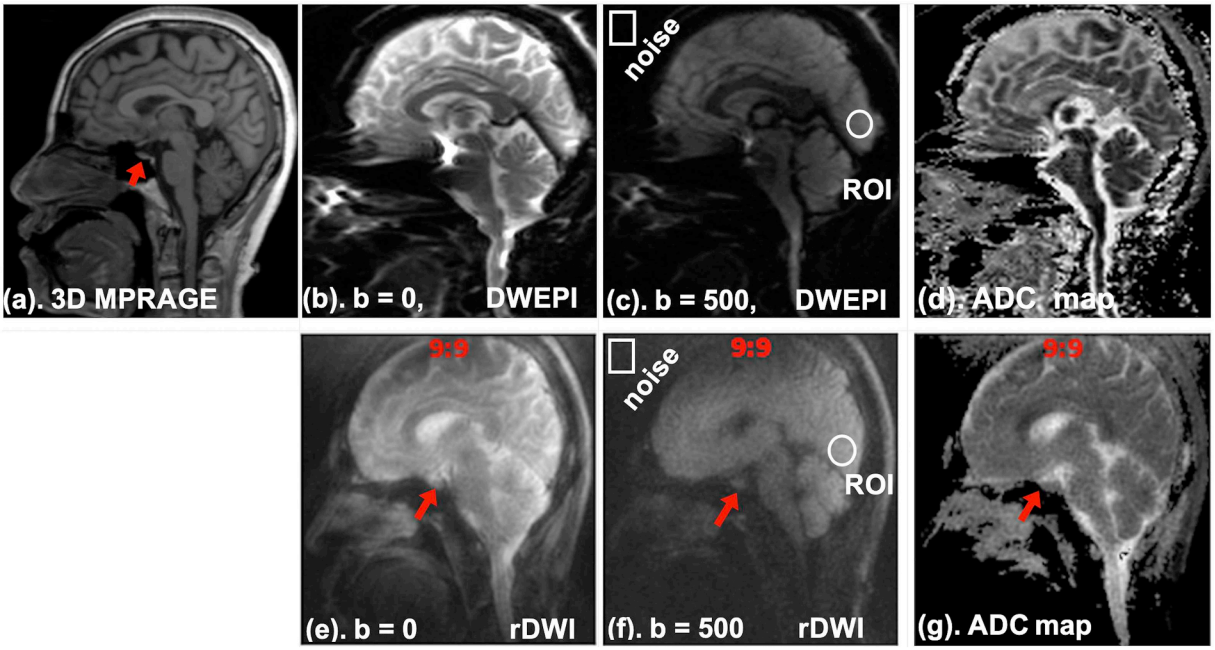

Fig. 10. In-vivo human brain DW images of sagittal plane: (a) anatomical image, (b–d) 2D ss-DWEPI, and (e–g) 2D ss-rDWI with b = (b, e) 0, (c, f) 500 s/mm^2 and (d, g) corresponding ADC map. The pituitary gland (indicated by arrows) is visible in 2D ss-rDWI. However, it is not possible to identify pituitary gland on images obtained using 2D ss-DWEPI because of severe susceptibility-induced geometric distortion. ROIs to estimate the SNR are shown in (c) and (f).

box in b = 500 s/mm^2 images. Note that the image acquisition times are 16 and 80 s for 2D ss-DWEPI and 2D ss-rDWI, respectively.

4. Discussion

A steady-state MRI relies on fresh longitudinal magnetization being recovered during each echo spacing [2,3]. However, only the diffusion-prepared magnetization must contribute to the measured signal in diffusion-MRI. This is the main cause of low SNR in any gradient-echo based DWI, including current rDWI. Recent advances in MRI systems include increased gradient strength, particularly helpful for diffusion MRI. For instance, one can reduce the diffusion gradient duration δ by half in the system with doubled gradient strength for the same separation Δ and b-factor. The echo time TE is also reduced accordingly, hence reducing the T_2 decay-related signal reduction in the resultant DWI.

The amount of the diffusion-prepared longitudinal magnetization M_z^D decreases over the echo train in diffusion-prepared radial imaging because of (i) increased T_1 decay with increased TM until each partial excitation RF and (ii) continual consumption for the imaging. For

instance, the available $M_z^D(t)$ is much smaller for the later projection because of greater T_1 decay due to the longer TM and previous usages. Numerical simulation and experimental data, which are shown in Fig. 6, clearly indicate that while the rDWI measured using the VFA scheme provides optimal signal intensity over a wide range of initial flip angles α_1. The signal intensity using CFA increases with increased flip angles up to $\alpha = \sim 15^o$, which is much larger than the optimal flip angle α_1^{opt} for VFA; however, image distortion is significantly increased at this large flip angle with the SVO, as shown in the simulated and experimental images in Figs. 4 and 7. VFA scheme allows to consume all diffusion-prepared longitudinal magnetization for maximum SNR, and RVO induces the least distortion.

As eq. [2] indicates, the initial flip angle for optimal SNR with reduced geometric distortion in the VFA scheme depends on T_1 relaxation time and the spacing between two consecutive RF pulses. The difference in flip angles for different T_1s will be smaller with shorter echo spacing. Therefore, it is desirable to minimize the echo spacing, such as using high receiver bandwidth. A minimal spoiling gradient after data acquisition may be used in combination with more vibrant jump between two adjacent radial spoke directions, of which a readout gradient spoils any coherent transverse magnetization from previous readout. For instance, using the echo spacing 3.0 ms, α_1^{opt} is calculated as 7.1°, 7.5°, and 7.9° for T_1 = 0.5, 1.0, and 1.5 s, respectively, in which the initial flip angle 7.5° may be adequate for this T_1 range. A concern for this method may be an increased eddy-current-related artifact.

The transverse magnetization varies along the echo train in this 2D ss-rDWI, i.e., along the angular direction, when using CFA and VFA with a non-optimal initial flip angle, particularly using the SVO scheme. This results in relatively higher signal intensity close to $k_\theta = 0^o$ line, either at the fourth or first quadrant for small or large initial flip angle, respectively. This varying echo amplitude causes blurring and geometric shearing on the resultant image along the angular direction, as shown in Figs. 1, 2, 3, and 7. Blurring and shearing distortions are reduced using the VFA with RVO scheme, as predicted by the point-spread function analysis, and both simulation and experiment.

Multi-shot diffusion MRI requires the minimal phase inconsistency or a robust phase-correction among different averaging shots, otherwise motion-induced phase inconsistency induces a shading or ghosting artifact on the resultant images. Although current DWI using radial sampling may experience less motion artifact than the Cartesian imaging, the inconsistent phase error is caused during the diffusion-preparation differently for different single-shot data. Therefore, complex averaging over multiple shots of data is not desirable. Also, radial DWI using sliding coverages produced images with reduced streak artifacts compared with images measured using the identical coverages.

As demonstrated in in-vivo DWI in Figs. 9 and 10, even with no noticeable geometric distortion, application of 2D ss-rDWI may be limited by its low SNR, which is caused by sharing the diffusion-prepared longitudinal magnetization by multiple RF pulses. SNR of the 2D ss-rDWI can be improved by acquiring longer radial trajectory, such as multiple spokes or spiral trajectory, instead of measuring a single radial spoke after each excitation RF pulse as in the current method. Then, for a similar k-space data sampling, a reduced number of RF pulses is applied with increased flip angle, which will result in increased signal intensity with the expense of increased geometric distortion due to the longer readout duration. Because the geometric distortion on images acquired using 2D ss-DWEPI linearly increases with the static field strength, 2D ss-rDWI may be particularly useful at high-field MRI system, such as 7 T MRI, with the added benefit that SNR will be naturally increased.

In summary, 2D ss-rDWI produces DW images with (a) no motion-related ghosting artifact owing to heavy sampling at k_o point, (b) maximized SNR by consuming all diffusion-prepared magnetization using variable flip angle in each shot, and (c) reduced geometric shearing using randomized viewordering. Although 2D ss-rDWI may not replace 2D ss-DWEPI for DWI and DTI of intracranial brain, because of low SNR, it may become a useful tool for DWI of brain at the skull base near the sinus and temporal bone and other organs outside the brain. Also, current technique may be useful for DWI at higher field MRI system, such as 7 T, at where the measured SNR and degree of geometric distortion are increased with the field strength and the geometric distortion on the EPI-based imaging is more problematic.

5. Conclusions

We present a 2D single-shot diffusion-weighted MRI method using the radial sampling (2D ss-rDWI). Because the entire k-space data is measured using a gradient-echo type reading after a single diffusion-preparation, 2D ss-rDWI suffers from low SNR and shearing artifact. SNR is maximized using the variable flip angle, and the image shearing was minimized using the randomized spoke ordering. The resultant DW images are insensitive to the susceptibility- and motion-induced artifacts, particularly for quantitative analysis.

Acknowledgements

This work was supported by NIH 1R56NS106097-01A1 and S10OD018482, Research Grants CA160725040 and RG5233-A-2 from National Multiple Sclerosis Society, and Alice and Kevin Steiner.

Appendix 1. How is stimulated echo is formed

Consider a pulse sequence, as shown in Fig. 1, which measures a diffusion-weighted stimulated-echo at an effective echo time, $TE = TE_D + TE_1$,

$$[90^o_{exc} - G_D - 180^o - G_D - G^d_{cr} - 90^o_{tipup}] - G_{spoil}\cdots TM_o\cdots - \alpha_1 - G^r_{cr} - ACQ \tag{A1}$$

with $TE_D + TE_1/2$ between $90_{exc}{}^o$ and $90_{tipup}{}^o$, TM_o between $90_{tipup}{}^o$ and the first investigatory RF α_1, and $TE_1/2$ between α_1 and $k_r = 0$ during ACQ. Two diffusion gradient pulses with durations δ are separated by Δ, which gives b value, $b = (\gamma G_D \delta)^2(\Delta - \delta/3)$. The diffusion-weighted and dephased (by the dephasing crusher gradient $G_{cr}{}^d$) transverse magnetization at the peak of $90_{tipup}{}^o$, before being tipped up, can be described as,

$$M_+(TE_D + TE_1/2) = M_o e^{-\left(TE_D + \frac{TE_1}{2}\right)/T_2} e^{-bD} e^{-i\theta^d_{cr}(\vec{r})}, \tag{A2}$$

where $\theta^d_{cr}(\vec{r}) = \gamma \int \vec{G}^d_{cr}(t)\cdot\vec{r}\ dt$. The $90_{tipup}{}^o$ tips up cosine comonent of this transverse magnetization into the longitudinal space, i.e., parallel to the external magnetic field $\vec{B_o}$. Immediately after the tip up RF pulse, remaining transverse component is spoiled by a large spoiling gradient G_{spoil}. The z-component becomes,

$$M^D_z(TM = 0) = M^D_z\left(t = TE_D + \frac{TE_1}{2}\right) = M_+\left(TE_D + \frac{TE_1}{2}\right)\cos\theta^d_{cr}(\vec{r}) \tag{A3}$$

During the mixing time TM_o, this diffusion-weighted magnetization undergoes a T_1 decay, while a freshly magnetization grows as,

$$M_z(TM) = M_z^D(TM=0)\cdot e^{-\frac{TM_o}{T_1}} + M_o\left(1 - e^{-\frac{TM_o}{T_1}}\right) \tag{A4}$$

Here, the first and second terms represent the diffusion-weighted magnetization undergoing T_1 decay and freshly recovering magnetization, respectively. The first investigatory RF pulse with a flip angle α_1 tips a sine component to the transverse plane as, $M_+(\alpha_1) = M_z(TM_o)\sin\alpha_1$ and followed by the rephasing crusher gradient $G_{cr}{}^r$, which imposes an additional phase $\theta_{cr}^r(\vec{r}) = \gamma\int \vec{G}_{cr}^r(t)\cdot\vec{r}\ dt = \theta_{cr}^d(\vec{r})$ to the transverse magnetization.

$$M_+(\alpha_1, G_{cr}^r) = M_+\left(TE_D + \frac{TE_1}{2}\right)e^{-\frac{TM_o}{T_1}}\cos\theta_{cr}^d(\vec{r})\cdot e^{-i\theta_{cr}^r(\vec{r})}\sin\alpha_1 \tag{A5}$$

Here, $\cos\theta_{cr}^d(\vec{r})\cdot e^{-i\theta_{cr}^r(\vec{r})} = 0.5(e^{i\theta_{cr}^d(\vec{r})} + e^{-i\theta_{cr}^d(\vec{r})})e^{-i\theta_{cr}^r(\vec{r})} = 0.5(1 + e^{-i2\theta_{cr}^d(\vec{r})})$, of which the second term is further dephased and canceled during the vector summation over entire isochromats within an imaging voxel as, $signal = \Sigma_{entire\ voxel}M_+(\alpha_1, G_{cr}{}^r)$. A stimulated-echo is formed at the time $TE_1/2$ after each RF pulse α_1 with the amplitude,

$$M_+(\alpha_1, G_{cr}^r) = 0.5M_+\left(TE_D + \frac{TE_1}{2}\right)e^{-\frac{TM_o}{T_1}}e^{-\frac{TE_1}{2}}\sin\alpha_1 = 0.5M_o e^{-\frac{(TE_D+TE_1)}{T_2}}e^{-\frac{TM_o}{T_1}}e^{-bD}\sin\alpha_1 \tag{A6}$$

Note that a half of the diffusion-prepared magnetization is lost while tipping up, which is a disadvantage of all stimulated-echo NMR. The transverse magnetization after n$^{\underline{th}}$ RF pulse α_n is,

$$M_+^n(\alpha,\tau) = 0.5M_o e^{-\frac{(TE_D+TE_1)}{T_2}}e^{-\frac{TM_o}{T_1}}e^{-bD}\left(\prod_{m=0}^{n-1}\cos\alpha_m\ e^{-\tau/T_1}\right)\sin\alpha_n \tag{A7}$$

The term $\prod_{m=0}^{n-1}\cos\alpha_m\ e^{-\tau/T_1}$ reflects continual consumption and T_1 decay of the diffusion prepared longitudinal magnetization, until a portion is flip to the transverse place.

Appendix 2. 1D point-spread function (PSF) analysis

The amplitude of the transverse magnetization after nth RF pulse α_n is described as,

$$M_+^n(\alpha,\tau) = \left(\prod_{m=0}^{n-1}\cos\alpha_m\ e^{-\tau/T_1}\right)\sin\alpha_n. \tag{A8}$$

The modulation transfer function, MTF, is obtained by ordering this transverse magnetization for specific view ordering, as $MTF(k_\phi) = M_+{}^n(\alpha,\tau)$ [vieworder(ϕ)]. This transverse magnetization is distributed along the angular path (k_ϕ) with viewordering in SVO or RVO scheme, generating MTFsvo and MTFrvo, respectively, as shown in Fig. A1a. The direct Fourier-Transformation of this MTF leads to a PSF, representing a point blurring along the angular direction, as shown in Fig. A1b. Echo train length (ETL) of 256 is used for Fig. A1(b, c) to better illustrate the broadening effect. Plots in Fig. A1c indicate that the full-width half-maximum (FWHM) is maintained low using RVO for both flip angle schemes.

Using the initial flip angle $\alpha_1 = 7.5^\circ$ which is the optimal α_1 for $T_1 = 1.0$ s, MTF is calculated for $T_1 = 0.4$, 0.75, 1.0, and 1.5 s using Fig. A2(a) VFA and A2(b) CFA. $\alpha_1{}^{opt}$ are 6.4°, 7.3°, 7.5°, and 7.8° for 0.4, 0.75, 1.0, and 1.5 s, respectively. These values of T_1 are those of fat proton and tissue water protons at 3 T. As their optimal initial flip angles differ less than 7% for $T_1 = 0.75$, 1.0, and 1.5 s, MTFs of T_1 0.75 and 1.5 s do not deviate that of $T_1 = 1.0$ s. Solid lines and symbols represent for SVO and RVO, respectively. For the range of T_1 (0.75–1.5 s), the transverse magnetization is much more scattered using CFA than using VFA. The SNR was estimated by averaging MTF values along the echotrain for each flip angle scheme and plotted with respect to the initial flip angle α_1 in Fig. A2c. Note that the SNR is determined by that of k_o data, which is averaged over all radial data during the regridding process.

Appendix 3. Comparison of flip angle and vieworder schemes for human brain rDWI

Images in Fig. A3 are obtained from a healthy human volunteer using different combinations of flip angle, viewodering, and initial flip angle α_1. SNRs are measured at the pituitary gland and occipital lobe, as indicated in Fig. A3e and listed in Table 1. The geometric shearing, which are shown in simulated images in Fig. 4 and measured images in Fig. 7, are not visually obvious, probably because of heterogeneity in water proton T_1 relaxation times in brain tissue. However, SNR stays high with VFA with the optimal $\alpha_1{}^{opt}$, as illustrated in Figs. 6 and A2c.

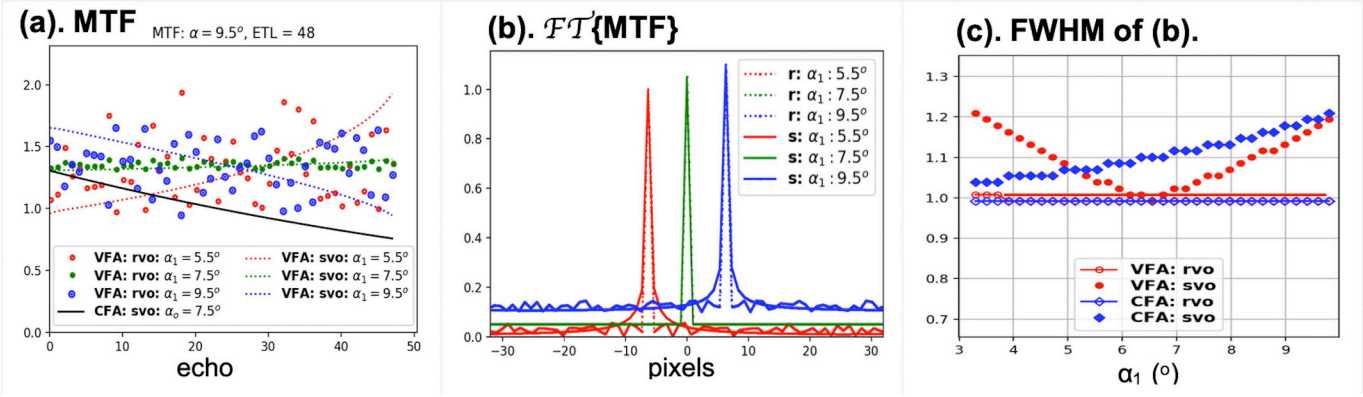

Fig. A1. (a). MTF (lines for SVO and circles for RVO) vs. echo number, (b). FFT{MTF} vs. pixel for VFA with optimal initial flip angle (green, $\alpha_1{}^{opt} = 7.5^\circ$) and

deviated angles (red/5.5° and blue/9.5°), plotted in dotted (RVO) and solid (SVO) lines, (c). full-width half-maximum, measured from (b), and shear along the angular direction for initial flip angle α_1 = 5.5 (red), 7.5 (green), and 9.5° (blue). The optimal initial FA is estimated as 7.5° for ETL 48 with τ/T_1 = 0.003. Plots in (c) indicates that point-blurring is minimized by using RVO, but optimal with VFA and RVO combination. (For interpretation of the references to colour in this figure legend, the reader is referred to the web version of this article.)

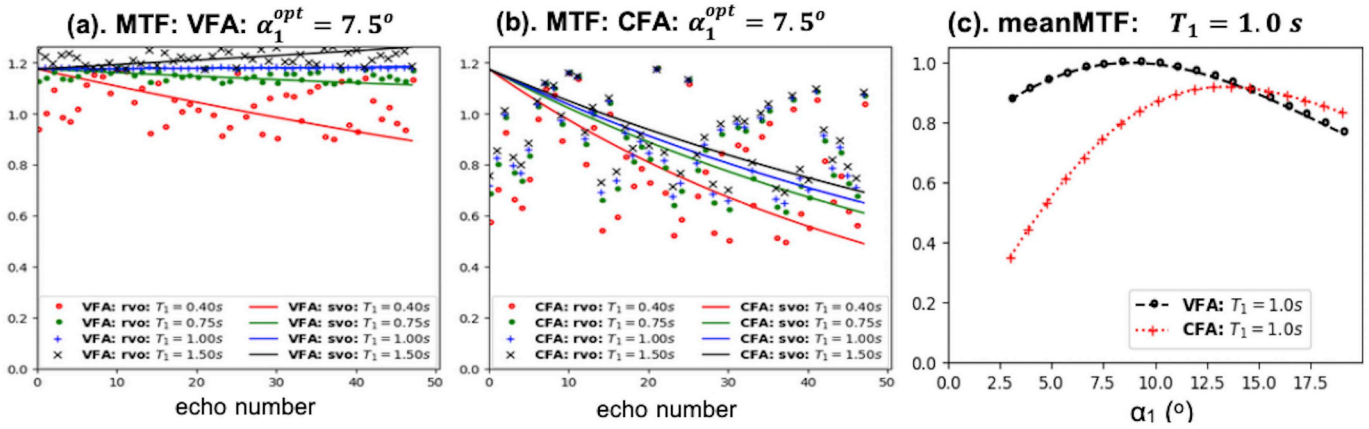

Fig. A2. Magnetization Transfer Functions (MTF) for T_1 0.4, 0.75, 1.0, and 1.5 s using (a) VFA and (b) CFA using α_1 = 7.5° which is the optimal initial flip angle for T_1 = 1.0 s. α_1^{opt} are 6.4°, 7.3°, 7.5°, and 7.8° for 0.4, 0.75, 1.0, and 1.5 s, respectively. Solid lines and symbols represent for SVO and RVO, respectively. For the range of T_1 (0.75–1.5 s), the transverse magnetization is much more scattered using CFA than VFA. Plots in (c) represents the expected SNR with respect to the initial flip angles for VFA (●) and CFA (+).

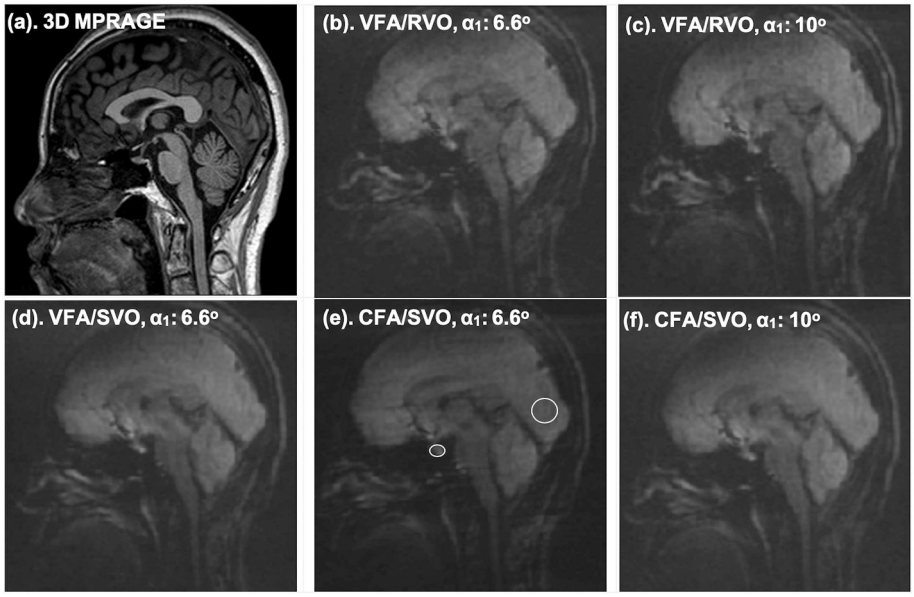

Fig. A3. The reference T1WI (a) and DWIs (b–e) of brain with b = 500 s/mm^2 using different combinations of flip angle scheme, initial flip angle, and viewordering. For images (b–e), the same window level and width are used, so the brightness indicates the relative signal intensity. Signal intensity is high using VFA compared with CFA. Because of heterogeneity of T_1, geometric shearing is not visibly clear.

References

[1] Jeong EK, Guo J, Kholmovski EG, Parker DL. High-resolution DTI with 2D interleaved multislice reduced FOV single-shot diffusion-weighted EPI (2D ss-rFOV-DWEPI). Magn Reson Med 2005;54:1575–9. https://doi.org/10.1002/mrm.20711.

[2] M a Bernstein, King KE, Zhou XJ, Fong W. Handbook of MRI pulse sequences. 2005. https://doi.org/10.1118/1.1904597.

[3] Haacke EM, Brown RW, Thompson MR, Venkatesan R. Haacke - magnetic resonance imaging - physical principles and sequence design.pdf. 1999. https://doi.org/10.1063/1.3554697.

[4] Sapkota N, Shi X, Shah LM, Bisson EF, Rose JW, Jeong EK. Two-dimensional single-shot diffusion-weighted stimulated EPI with reduced FOV for ultrahigh-b radial diffusion-weighted imaging of spinal cord. Magn Reson Med 2016. https://doi.org/10.1002/mrm.26302.

[5] Turner R, Le Bihan D, Maier J, Vavrek R, Hedges LK, Pekar J. Echo-planar imaging of intravoxel incoherent motion. Radiology 1990;177:407–14. https://doi.org/10.1148/radiology.177.2.2217777.

[6] Chen N, Guidon A, Chang HC, Song AW. A robust multi-shot scan strategy for high-resolution diffusion weighted MRI enabled by multiplexed sensitivity-encoding (MUSE). Neuroimage 2013;72:41–7. https://doi.org/10.1016/j.neuroimage.2013.01.038.

[7] Schenck JF. The role of magnetic susceptibility in magnetic resonance imaging: MRI magnetic compatibility of the first and second kinds. Med Phys 1996;23:815–50. https://doi.org/10.1118/1.597854.

[8] Korn N, Kurhanewicz J, Banerjee S, Starobinets O, Saritas E, Noworolski S. Reduced-FOV excitation decreases susceptibility artifact in diffusion-weighted MRI with endorectal coil for prostate cancer detection. Magn Reson Imaging 2015;33:56–62. https://doi.org/10.1016/j.mri.2014.08.040.

[9] Pipe JG, Farthing VG, Forbes KP. Multi-shot diffusion-weighted FSE using PROPELLER MRI. Magn Reson Med 2002;47:42–52. https://doi.org/10.1002/mrm.10014.

[10] Porter DA, Heidemann RM. High resolution diffusion-weighted imaging using readout-segmented echo-planar imaging, parallel imaging and a two-dimensional

navigator-based reacquisition. Magn Reson Med 2009;62:468–75. https://doi.org/10.1002/mrm.22024.
[11] Li TQ, Kim DH, Moseley ME. High-resolution diffusion-weighted imaging with interleaved variable-density spiral acquisitions. J Magn Reson Imaging 2005;21:468–75. https://doi.org/10.1002/jmri.20287.
[12] Truong TK, Guidon A. High-resolution multi-shot spiral diffusion tensor imaging with inherent correction of motion-induced phase errors. Magn Reson Med 2014;71:790–6. https://doi.org/10.1002/mrm.24709.
[13] Jeong K, Hsu E, Jeong E. 2D single-shot radial diffusion-weighted imaging free of geometric distortion and optimization of SNR using variable flip-angle and random view-ordering (1642). Annual meeting of ISMRM – ESMRMB 2018, Paris, France. 2018.
[14] Theilmann RJ, Gmitro AF, Altbach MI, Trouard TP. View-ordering in radial fast spin-echo imaging. Magn Reson Med 2004;51:768–74. https://doi.org/10.1002/mrm.20031.
[15] Saritas EU, Cunningham CH, Lee JH, Han ET, Nishimura DG. DWI of the spinal cord with reduced FOV single-shot EPI. Magn Reson Med 2008;60(2):468–73. https://doi.org/10.1002/mrm.21640.
[16] Jeong EK, Kholmovski EG, Parker DL. High-resolution DTI of a localized volume using 3D single-shot diffusion-weighted stimulated echo-planar imaging (3D ss-DWSTEPI). Magn Reson Med 2006;56:1173–81. https://doi.org/10.1002/mrm.21088.
[17] Zhang S, Block KT, Frahm J. Magnetic resonance imaging in real time: advances using radial FLASH. J Magn Reson Imaging 2010;31:101–9. https://doi.org/10.1002/jmri.21987.
[18] Bi X, Park J, Larson AC, Zhang Q, Simonetti O, Li D. Contrast-enhanced 4D radial coronary artery imaging at 3.0 T within a single breath-hold. Magn Reson Med 2005;54:470–5. https://doi.org/10.1002/mrm.20575.
[19] Jeong EK, Parker DL. High-resolution diffusion-weighted 3D MRI, using diffusion-weighted driven-equilibrium (DW-DE) and multi-shot segmented 3D-SSFP without navigator echoes. Magn Reson Med 2003;50:821–9. https://doi.org/10.1002/mrm.10593.
[20] Baddour N. Two-dimensional Fourier transforms in polar coordinates. Adv Imaging Electron Phys 2011;165:1–45. https://doi.org/10.1016/B978-0-12-385861-0.00001-4.
[21] Jeong EK, Parker DL, Tsuruda JS, Won JY. Reduction of flow-related signal loss in flow-compensated 3D TOF MR angiography, using variable echo time (3D TOF-VTE). Magn Reson Med 2002;48:667–76. https://doi.org/10.1002/mrm.10258.
[22] Aaron M, Smith CP, Paprocki M, et al. SymPy: symbolic computing in Python. PeerJ Comput Sci 2017;3:e103.
[23] Van Der Walt S, Colbert SC, Varoquaux G. The NumPy array: a structure for efficient numerical computation. Comput Sci Eng 2011;13:22–30. https://doi.org/10.1109/MCSE.2011.37.
[24] Oliphant TE. SciPy: open source scientific tools for Python. Comput Sci Eng 2007;9:10–20. https://doi.org/10.1109/MCSE.2007.58.
[25] Hunter JD. Matplotlib: a 2D graphics environment. Comput Sci Eng 2007;9:99–104. https://doi.org/10.1109/MCSE.2007.55.
[26] Nielles-Vallespin S, Weber MA, Bock M, Bongers A, Speier P, Combs SE, et al. 3D radial projection technique with ultrashort echo times for sodium MRI: clinical applications in human brain and skeletal muscle. Magn Reson Med 2007;57:74–81. https://doi.org/10.1002/mrm.21104.
[27] Jackson JI, Meyer CH, Nishimura DG, Macovski A. Selection of a convolution function for Fourier inversion using gridding. IEEE Trans Med Imag 1991;10:473–8.
[28] Johnson KO, Pipe JG. Convolution kernel design and efficient algorithm for sampling density correction. Magn Reson Med 2009;61:439–47. https://doi.org/10.1002/mrm.21840.